energies

MDPI

Article

A New Approach of Minimizing Commutation Torque Ripple for BLDCM

Bo Tan [1,*], Zhiguang Hua [1], Lu Zhang [2] and Chun Fang [1]

[1] Shaanxi Key Laboratory of Small & Special Electrical Machine and Drive Technology, Northwestern Polytechnical University, Xi'an 710072, China; h_zhiguang@163.com (Z.H.); chunfang@mail.nwpu.edu.cn (C.F.)

[2] Xi'an Flight Automatic Control Research Institute, Xi'an 710065, China; plzl0601@163.com

* Correspondence: tanbo345@163.com; Tel.: +86-029-8843-1310

Received: 21 August 2017; Accepted: 26 October 2017; Published: 30 October 2017

Abstract: The properties of brushless DC motor (BLDCM) are similar to the fractional, slot-concentrated winding of permanent-magnet synchronous machines, and they fit well for electric vehicle application. However, BLDCM still suffers from the high commutation torque ripple in the case of the traditional square-wave current control (SWC) method, where the current vector rotates asynchronously with back-EMF. A current optimizing control (COC) method for BLDCM is proposed in the paper to minimize the commutation torque ripple. The trajectories of the three phase currents are planned by the given torque and the optimized result of the copper loss and motor torque equations. The properties of COC are analyzed and compared with that of SWC in the stationary reference frame. The results show that the way of making the current vector rotate synchronously with back-EMF (back-Electromotive Force) can minimize the modulus and velocity of the current vector in the commutation region, and reduce the torque ripple. Experimental tests obtained from an 82 W BLDCM are done to confirm the theoretical findings.

Keywords: BLDCM; commutation torque ripple; rotating synchronously; current optimizing control

1. Introduction

BLDCM with trapezoid wave back-EMF has been widely used in industry and civil equipment due to its advantages of high torque and power density, and low inverter capacity demand [1]. BLDCM is particularly suitable for applications with rigorous requirements on weight, space, and efficiency, such as electric vehicles. Its properties are similar to fractional slot-concentrated winding permanent magnet synchronous machines. However, BLDCM has the disadvantage of high commutation torque ripple in the traditional square-wave current control method, which increases the operating noise and reduces the torque control precision. These problems limit the application of BLDCM in electric vehicles and servo systems.

The main studies on reducing the commutation torque ripple include overlap commutation, two-phase and three-phase conduction modes combination, adding power supply circuits in front of the three phase inverter, modifying power topology, decoupling control, and the sinusoidal current supply [2–11]. Overlapping commutation and duty pulse width modulation (PWM) optimization are adopted to reduce the torque ripple in [2]. Each period of PWM is divided into three segments during commutation time, and it is selected properly to reduce the commutation torque ripple [3]. The commutation torque ripple is reduced by commutation control with the two-phase switching mode or the three-phase switching mode [4]. The optimal switching status is generated according to the established predictive model to reduce the commutation torque ripple [5]. A method of Z-source inverter-fed BLDCM is proposed in [6], which can reduce the commutation torque ripple by regulating the duty cycle of the shoot-through vector and the active vector. A novel inverter topology, which can

supply higher dc-link voltage for the freewheeling phase and reduce commutation time, is presented [7]. In [8], the three-level inverter is combined with the single-ended primary-inductor converter (SEPIC) to reduce the current and torque ripples. The electromagnetic torque can be controlled by the q axis component of the current vector [9]. The work in [10] minimizes the torque ripple by selective elimination of torque harmonics achieved through the supply of the motor phases with a sinusoidal-like current waveform. The sinusoidal current supply outperforms the real square-wave current supply over almost the speed range [11]. Summarizing the above studies, it can be concluded that the overlap commutation and conduction modes combination will extend commutation time, increase switching losses, and decrease efficiency [4]. Adding power supply circuits or modifying the power topology will make the power current and control method complex, and decrease the reliability of the driver. The trapezoidal phase back-EMFs of BLDCM are rich in harmonics. However, the characters of the trapezoidal phase back-EMFs may not be reflected in the decoupling control, because the complex process of decoupling for high order harmonics is usually neglected. It is worth mentioning that the harmonic components of the back-EMF, apart from being the fundamental component, do not give any contribution to the active electric power when the current is sinusoidal but just determine the torque ripple of the BLDCM [11].

In the premise of the three phase inverter topology and the non-decoupling strategy, a current optimizing control method for BLDCM is proposed in the paper to minimize the commutation torque ripple. The trajectories of the three phase currents are calculated by the given torque and the optimized result of copper loss and motor torque equations. Although other papers have already dealt with the current optimizing method for BLDCM, the decoupling control involving the d q synchronous frame is always adopted in analyses or experiments [12–16]. Unlike the work above, this paper provides a current optimizing method in the natural a–b–c reference frame and its properties are compared with the traditional method. Experimental results are carried out to verify the proposed method.

2. Description of the Traditional SWC

Torque equation of BLDCM is:

$$T_{em} = \frac{e_a i_a + e_b i_b + e_c i_c}{\Omega} \tag{1}$$

where T_{em} is electromagnetic torque; Ω is electrical angular velocity of rotor; i_a, i_b and i_c are three-phase currents; and e_a, e_b and e_c are three-phase back-EMF. With the changes of the back-EMF, the rotor position can be divided into 6 sectors as shown in Figure 1. θ_r is electrical angle of rotor; E_ϕ is the amplitude of back-EMF flat-topped wave.

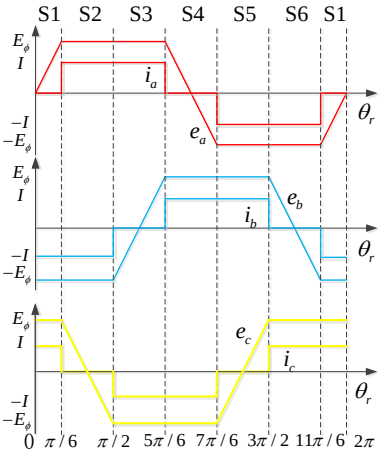

Figure 1. Ideal waveforms of back-EMF and phase current in square-wave current control (SWC).

In SWC, only two phases are conducted simultaneously. When the rotor position locates in the 4th sector, $i_a = 0$, $i_b = -i_c$, and $e_b = -e_c = E_\phi$. The torque equation is written as:

$$T_{em} = \frac{e_b i_b + e_c i_c}{\Omega} = \frac{2E_\phi i_b}{\Omega} = -\frac{2E_\phi i_c}{\Omega} \tag{2}$$

Assuming $C_T = E_\phi/\Omega$, i_a, i_b and i_c can be expressed as:

$$\begin{cases} i_a = 0 \\ i_b = T_{em}/2C_T = T_{em} \cdot i_b^* \\ i_c = -T_{em}/2C_T = T_{em} \cdot i_c^* \end{cases} \tag{3}$$

C_T is a constant value. The per-unit values of three phase currents are:

$$\begin{cases} i_a^* = 0 \\ i_b^* = 1/2C_T \quad 5\pi/6 < \theta_r \leq 7\pi/6 \\ i_c^* = -1/2C_T \end{cases} \tag{4}$$

Similarly, the per-unit values of three phase currents in the 5th sector are written as:

$$\begin{cases} i_a^* = -1/2C_T \\ i_b^* = 1/2C_T \quad 7\pi/6 < \theta_r \leq 3\pi/2 \\ i_c^* = 0 \end{cases} \tag{5}$$

In SWC, ideal wave of per phase current is square and with 120° non-conduction interval as shown in Figure 1. However, the non-commutation phase current will curve in for the different change rates of upcoming phase current and outgoing current during the commutation region, and the commutation torque ripple is induced. The difference is induced by limited current change rates which are restrained by the winding inductance, current path and voltage of the DC source. The main goal of overlap commutation and adding power supply circuits is to make the non-commutation phase current constant by keeping the current change rates equal in the commutation region.

3. Theory of the Proposed COC

If phase currents can keep conducting and changing synchronously with back-EMF in the 120° non-conduction interval, the phase currents will be continuous. The continuous currents, which can be realized by a lower current change rates, will avoid problems induced by the limited current change rates in SWC. So, the commutation torque ripple would be reduced.

When the rotor position is in the 4th sector, e_a, e_b and e_c can be expressed as:

$$\begin{cases} e_a = E(\theta_r) \\ e_b = E_\phi \quad 5\pi/6 < \theta_r \leq 7\pi/6 \\ e_c = -E_\phi \end{cases} \tag{6}$$

The sum of three phase currents is zero. Then, from Equation (6), we can find that:

$$T_{em} = \frac{E(\theta_r) i_a + E_\phi i_b + E_\phi (i_a + i_b)}{\Omega} \tag{7}$$

Assuming $C_T(\theta_r) = E(\theta_r)/\Omega$, the torque equation is written as:

$$T_{em} = (C_T(\theta_r) + C_T) i_a + 2C_T i_b \tag{8}$$

The copper loss equation is:

$$p_{Cu} = R[i_a^2 + i_b^2 + (i_a + i_b)^2] \tag{9}$$

where R is phase resistance. The partial derivative of i_a and i_b can be calculated as:

$$\begin{cases} \frac{\partial(p_{Cu})}{\partial i_a} = R[2i_a + 2i_b\frac{di_b}{di_a} + 2(i_a + i_b)(1 + \frac{di_b}{di_a})] = 0 \\ \frac{\partial(p_{Cu})}{\partial i_b} = R[2i_a\frac{di_a}{di_b} + 2i_b + 2(i_a + i_b)(1 + \frac{di_a}{di_b})] = 0 \end{cases} \tag{10}$$

From Equation (8) we find that:

$$\begin{cases} i_a = \frac{T_{em} - 2C_T i_b}{C_T(\theta_r) + C_T} \\ i_b = \frac{T_{em} - (C_T(\theta_r) + C_T) i_a}{2C_T} \end{cases} \tag{11}$$

With Equation (11), Equation (10) can be written as:

$$\begin{cases} p_{Cu}(i_a)' = 2i_a + 2i_b(-\frac{C_T(\theta_r) + C_T}{2C_T}) + 2(i_a + i_b)(1 - \frac{C_T(\theta_r) + C_T}{2C_T}) = 0 \\ p_{Cu}(i_b)' = 2i_a(-\frac{2C_T}{C_T(\theta_r) + C_T}) + 2i_b + 2(i_a + i_b)(1 - \frac{2C_T}{C_T(\theta_r) + C_T}) = 0 \end{cases} \tag{12}$$

From Equation (12), we get:

$$\begin{cases} i_a = T_{em}\frac{C_T(\theta_r)}{3{C_T}^2 + C_T(\theta_r)^2} = T_{em} \times i_a^* \\ i_b = T_{em}\frac{3C_T - C_T(\theta_r)}{2(3{C_T}^2 + C_T(\theta_r)^2)} = T_{em} \times i_b^* \\ i_c = -T_{em}\frac{3C_T + C_T(\theta_r)}{2(3{C_T}^2 + C_T(\theta_r)^2)} = T_{em} \times i_c^* \end{cases} \tag{13}$$

The per-unit values of three phase currents are given by:

$$\begin{cases} i_a^* = \frac{C_T(\theta_r)}{3{C_T}^2 + C_T(\theta_r)^2} \\ i_b^* = \frac{3C_T - C_T(\theta_r)}{2(3{C_T}^2 + C_T(\theta_r)^2)} \\ i_c^* = -\frac{3C_T + C_T(\theta_r)}{2(3{C_T}^2 + C_T(\theta_r)^2)} \end{cases} \quad 5\pi/6 < \theta_r \leq 7\pi/6 \tag{14}$$

When the rotor position is located in the 5th sector, the per-unit values of three phase currents can be derived as:

$$\begin{cases} i_a^* = -\frac{3C_T + C_T(\theta_r)}{2(3{C_T}^2 + C_T(\theta_r)^2)} \\ i_b^* = \frac{3C_T - C_T(\theta_r)}{2(3{C_T}^2 + C_T(\theta_r)^2)} \\ i_c^* = \frac{C_T(\theta_r)}{3{C_T}^2 + C_T(\theta_r)^2} \end{cases} \quad 7\pi/6 < \theta_r \leq 3\pi/2 \tag{15}$$

When the rotor position is located in the 6th sector, the per-unit values of three phase currents can be expressed as:

$$\begin{cases} i_a^* = -\frac{3C_T + C_T(\theta_r)}{2(3{C_T}^2 + C_T(\theta_r)^2)} \\ i_b^* = \frac{C_T(\theta_r)}{3{C_T}^2 + C_T(\theta_r)^2} \\ i_c^* = \frac{3C_T - C_T(\theta_r)}{2(3{C_T}^2 + C_T(\theta_r)^2)} \end{cases} \quad 3\pi/2 < \theta_r \leq 11\pi/6 \tag{16}$$

The per-unit values of the other 3 sectors can be calculated similarly. The waveforms of current and back-EMF are shown in Figure 2. Three phase currents are continuous without step changes.

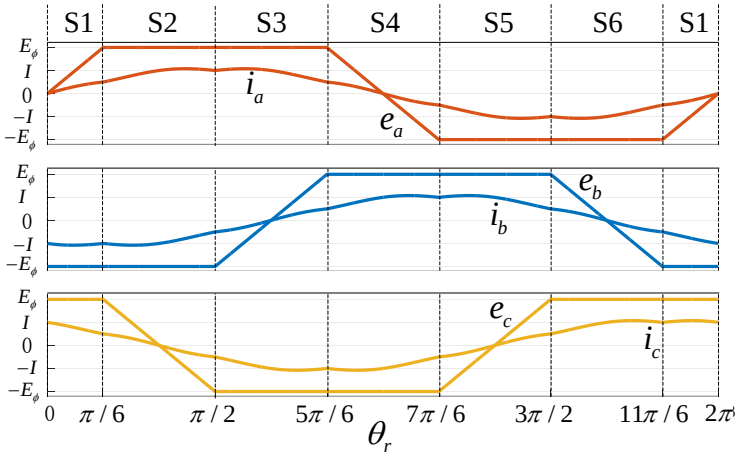

Figure 2. The waveforms of current and back-EMF.

4. Comparison of Commutation Torque Ripple

The commutation torque ripple of COC is analyzed and compared with traditional SWC in the stationary reference frame.

4.1. Square-Wave Control

When the rotor position is in the 4th sector, the phase current equations shown in Equation (4) are decomposed and considered as a vector in the stationary reference frame, then:

$$\begin{bmatrix} i_\alpha^* \\ i_\beta^* \end{bmatrix} = \frac{\sqrt{2}}{\sqrt{3}} \begin{bmatrix} 1, -\frac{1}{2}, -\frac{1}{2} \\ 0, \frac{\sqrt{3}}{2}, -\frac{\sqrt{3}}{2} \end{bmatrix} \begin{bmatrix} i_a^* \\ i_b^* \\ i_c^* \end{bmatrix} = \frac{\sqrt{2}}{\sqrt{3}} \begin{bmatrix} 0 \\ \frac{\sqrt{3}}{2C_T} \end{bmatrix} \tag{17}$$

Assuming current vector $i_{\alpha\beta}^* = \left[i_\alpha^*, i_\beta^*\right]$, the modulus of $i_{\alpha\beta}^*$ is:

$$i_m^* = \sqrt{i_\alpha^{*2} + i_\beta^{*2}} = \frac{1}{\sqrt{2}C_T} = 0.707/C_T \tag{18}$$

The angle θ_s of the current vector is $\pi/2$. So, the angular velocity Ω_s of the current vector is 0 in the 4th sector.

Back-EMF in the stationary reference frame is written as:

$$\begin{bmatrix} e_\alpha \\ e_\beta \end{bmatrix} = \frac{\sqrt{2}}{\sqrt{3}} \begin{bmatrix} 1, -\frac{1}{2}, -\frac{1}{2} \\ 0, \frac{\sqrt{3}}{2}, -\frac{\sqrt{3}}{2} \end{bmatrix} \begin{bmatrix} E(\theta_r) \\ E_\phi \\ -E_\phi \end{bmatrix} = \frac{\sqrt{2}\Omega}{\sqrt{3}} \begin{bmatrix} C_T(\theta_r) \\ \sqrt{3}C_T \end{bmatrix} \tag{19}$$

Assuming back-EMF vector $e_f = \left[e_\alpha, e_\beta\right]$, the modulus of back-EMF vector is:

$$e_m = \sqrt{e_\alpha^2 + e_\beta^2} = \frac{\sqrt{2}\Omega}{\sqrt{3}} \sqrt{3{C_T}^2 + C_T(\theta_r)^2} \tag{20}$$

When θ_r is π in the middle of the 4th sector, e_m is minimum. While, when θ_r is $7\pi/6$ in the commutation region, e_m is maximum:

$$\begin{cases} e_{m\_min} = \sqrt{2}\Omega C_T \approx 1.414\Omega C_T \\ e_{m\_\max} = 2\sqrt{2}\Omega C_T/\sqrt{3} \approx 1.633\Omega C_T \end{cases} \tag{21}$$

The angle of back-EMF vector is:

$$\theta_f = \arg\tan\frac{\sqrt{3}C_T}{C_T(\theta_r)} \tag{22}$$

$C_T(\theta_r)$ can be expressed as:

$$C_T(\theta_r) = 6(\pi - \Omega t)C_T/\pi \tag{23}$$

The angular velocity of the back-EMF vector is:

$$\Omega_f = \frac{18\pi\Omega}{\sqrt{3}(3\pi^2 + 36(\pi - \Omega t)^2)} \tag{24}$$

When θ_r is π in the middle of the 4th sector, Ω_f is maximum. While, when θ_r is $7\pi/6$ in the commutation region, Ω_f is minimum:

$$\begin{cases} \Omega_{f\_max} = 2\sqrt{3}\Omega/\pi \approx 1.103\Omega \\ \Omega_{f\_\min} = 3\sqrt{3}\Omega/2\pi \approx 0.827\Omega \end{cases} \tag{25}$$

The per-unit values value of torque can be expressed as:

$$T^*_{em} = e_f {i^*_{\alpha\beta}}^T/\Omega = e_m i^*_m \cos(\theta_f - \theta_s)/\Omega = \frac{\sqrt{2}}{\sqrt{3}}\sqrt{3{C_T}^2 + C_T(\theta_r)^2}\frac{1}{\sqrt{2}C_T}\frac{\sqrt{3}C_T}{\sqrt{3{C_T}^2 + C_T(\theta_r)^2}} = 1 \tag{26}$$

When the rotor is in the 5th sector, the three-phase current equation shown in Equation (5) is decomposed in the stationary reference frame, then:

$$\begin{bmatrix} i^*_\alpha \\ i^*_\beta \end{bmatrix} = \frac{\sqrt{2}}{\sqrt{3}}\begin{bmatrix} 1, -\frac{1}{2}, -\frac{1}{2} \\ 0, \frac{\sqrt{3}}{2}, -\frac{\sqrt{3}}{2} \end{bmatrix}\begin{bmatrix} i^*_a \\ i^*_b \\ i^*_c \end{bmatrix} = \frac{\sqrt{2}}{\sqrt{3}}\begin{bmatrix} -\frac{3}{4C_T} \\ \frac{\sqrt{3}}{4C_T} \end{bmatrix} \tag{27}$$

Its modulus is the same as Equation (18). The angle θ_s of the current vector is $5\pi/6$. The angular velocity Ω_s of the current vector is 0 in the 5th sector. However, Ω_s will be infinite in the commutation region for the step change of θ_s.

The similar study is carried out in the other sectors. The modulus, angular velocity and angle of current and back-EMF vector with SWC are shown in Figure 3, which are got according to the Equations (17)–(27). In the figure, the period of rotor electrical angle is set to 0.2 s, and the corresponding velocity of rotor is 31.4 rad/s.

In SWC, the properties of current and back-EMF vector are shown as follows.

(1) The modulus of current vector is a constant.
(2) The modulus of back-EMF vector is continuous and fluctuates with the angle of rotor. It is maximum in the commutation region, and minimum at the middle of sectors.
(3) The velocity of current vector is 0 in sectors, and infinite in the commutation region.
(4) The velocity of back-EMF vector is continuous and fluctuates with the angle of rotor. It is minimum in the commutation region, and maximum at the middle of sectors.
(5) Current vector rotates asynchronously with back-EMF.

In the commutation region, the torque can be ripple-free if the modulus of current vector is constant and its velocity is infinite. However, the constant modulus and infinite velocity can hardly be satisfied for the limited current change rates restricted by the winding inductance, different current path, the voltage of the DC source and the speed of controller. So, few paper focus on how to keep the velocity of current vector infinite and the modulus constant to make the torque ripple free in

the commutation region, because the actual current change rates cannot be infinite. And at present, most papers focus on keeping the change rates of currents equal to reduce commutation torque ripple. However, these methods cannot make the torque ripple free or minimum. So, a new driver method is necessary to solve the problems with SWC.

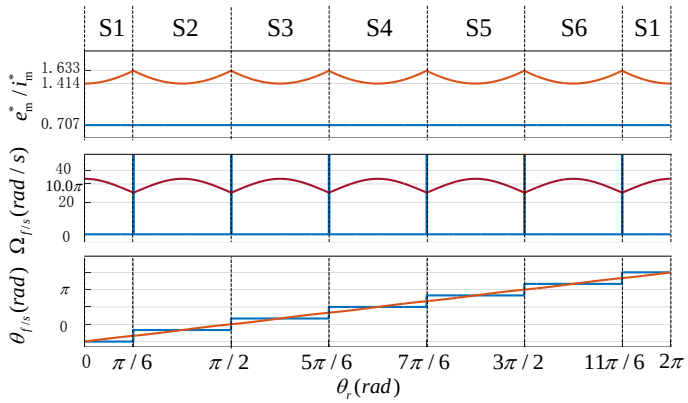

Figure 3. The waveforms of vector modulus, angular velocity, and angle with square-wave current control (SWC): (**up**) modulus of current vector (blue) and back-EMF (red); (**middle**) angular velocity of current vector (blue) and back-EMF vector (red); (**down**) angles of current vector (blue) and back-EMF vector (red).

4.2. Current Optimizing Control

When the rotor position is in the 4th sector, the phase current equations shown in Equation (14) are decomposed in the stationary reference frame, then:

$$\begin{bmatrix} i_\alpha^* \\ i_\beta^* \end{bmatrix} = \frac{\sqrt{2}}{\sqrt{3}} \begin{bmatrix} 1, -\frac{1}{2}, -\frac{1}{2} \\ 0, \frac{\sqrt{3}}{2}, -\frac{\sqrt{3}}{2} \end{bmatrix} \begin{bmatrix} i_a^* \\ i_b^* \\ i_c^* \end{bmatrix} = \frac{\sqrt{2}}{\sqrt{3}} \begin{bmatrix} \frac{3C_T(\theta_r)}{2(3C_T{}^2+C_T(\theta_r)^2)} \\ \frac{3\sqrt{3}C_T}{2(3C_T{}^2+C_T(\theta_r)^2)} \end{bmatrix} \tag{28}$$

The modulus of the current vector is:

$$i_m^* = \sqrt{i_\alpha^{*2} + i_\beta^{*2}} = \frac{\sqrt{3}}{\sqrt{2}\sqrt{3C_T{}^2 + C_T(\theta_r)^2}} \tag{29}$$

When θ_r is π in the middle of the 4th sector, i_m^* is maximum. When θ_r is $7\pi/6$ in the commutation region, i_m^* is minimum:

$$\begin{cases} i_{m\_max}^* = 1/\sqrt{2}/C_T \approx 0.707/C_T \\ i_{m\_min}^* = \sqrt{3}/2\sqrt{2}/C_T \approx 0.612/C_T \end{cases} \tag{30}$$

The angle θ_s of the current vector is the same as θ_f shown in Equation (22), and the velocity Ω_s of the current vector is the same as Ω_f shown in Equation (24).

The per-unit value of torque can be expressed as:

$$T_{em}^* = e_f i_{\alpha\beta}^{*\,T}/\Omega = e_m i_m^* \cos(\theta_f - \theta_s)/\Omega = \frac{\sqrt{2}}{\sqrt{3}}\sqrt{3C_T{}^2 + C_T(\theta_r)^2}\frac{\sqrt{3}}{\sqrt{2}\sqrt{3C_T{}^2 + C_T(\theta_r)^2}} = 1 \tag{31}$$

From Equations (20) and (29), the modulus of current and back-EMF vector is in inverse proportion. From Equations (22) and (24), the angle and velocity of current and back-EMF vector are synchronize. The velocity and modulus of current vector are minimum at the commutation time From Equations (25) and (30). From Equation (31), the dot product of current vector and back-EMF vector equals 1, and

commutation torque is ripple-free. The modulus, angular velocity, and angle of current and back-EMF vector with COC are shown in Figure 4, which are got according to the Equations (28)–(31). In the figure, the period of rotor angle is also set to 0.2 s, the rotor angular velocity is 31.4 rad/s, the angular velocity and the angles of current vector and back-EMF vector are the same (blue cannot be displayed).

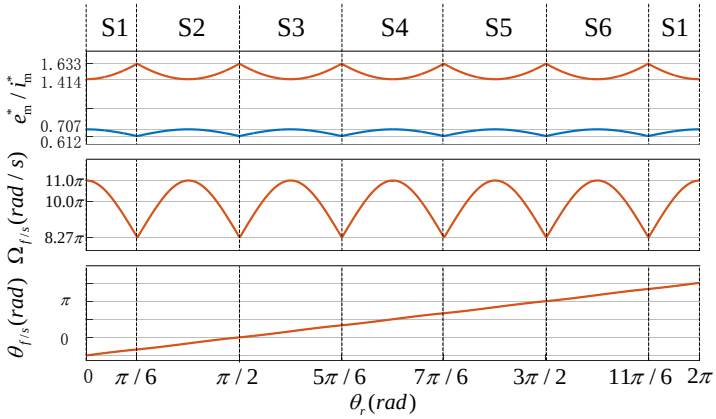

Figure 4. The waveforms of vector modulus, angular velocity, and angle with current optimizing control (COC): (**up**) modulus of current vector (blue) and back-EMF (red); (**middle**) angular velocity of current vector (blue) and back-EMF vector (red); (**down**) angles of current vector (blue) and back-EMF vector (red).

In COC, the properties of current and back-EMF vector are shown as follows:

(1) The modulus of current vector is continuous and fluctuates with the angle of rotor. It is maximum at the middle of sectors, and minimum in the commutation region.
(2) The velocity of current vector is continuous and fluctuates with the angle of rotor. It is maximum at the middle of sectors, and minimum in the commutation region.
(3) Current vector rotates synchronously with back-EMF vector, the modulus of these vectors are in inverse proportion, and the angles and velocities are the same.

When the angle of rotor is $7\pi/6$ in the commutation point of the 4th sector, the properties of current and back-EMF vector are shown in Table 1. Compared with SWC, the modulus of current vectors is decreased by 13.4%, and the velocity accounting for 82.7% of Ω is limited in COC. The inner power factor angle is $\pi/6$ in SWC, while it is 0 in COC.

Table 1. The properties of current vector and back-EMF when $\theta_r = 7\pi/6$.

Type	Modulus	Velocity	Angle
Current vector of SWC	$0.707/C_T$	$+\infty$	$\pi/2$
Current vector of COC	$0.612/C_T$	0.827Ω	$2\pi/3$
Back-EMF vector	$1.633\Omega C_T$	0.827Ω	$2\pi/3$

It can be seen that, the lowest modulus and limited velocity of current vector with COC in the commutation region reduce the demands of high current change rate. The contradiction between limited current change rate and the infinite velocity and higher modulus of current vector with SWC in the commutation region can be avoided. So, COC method has a natural advantage in terms of commutation torque ripple suppression.

5. Experiments

5.1. Experiment Setup

The experiment platform shown in Figure 5 is consisted of BLDCM, driver board, voltage source, computer, torque loading and power analyzer. The specifications of BLDCM are shown in Table 2.

Figure 5. The experiment platform.

Table 2. Specifications of the brushless DC motor (BLDCM).

Specification	Value
Rated voltage	24 V
Rated torque	0.2 Nm
Rated Velocity	3950 r/min
Rated current	5 A
Rated power	82 W
Torque coefficient	0.0475 Nm/A
Resistance of phase	0.49 Ω
Inductance of phase	0.16 mH
Numbers of pole pairs	2

In the experiment, the voltage of DC source is kept constant, the reference speed is set by computer, and the load is regulated by torque loading. Torque is measured by sensor in torque loading. Current waveforms and torque are recorded by power analyzer. In driver board, double closed-loop (velocity loop outside, current loop inside) control strategy is adopted. Traditional PI control strategy is used in the velocity loop. COC and SWC method are adopted in the current loop. The control diagrams of COC and SWC are shown in Figures 6 and 7 respectively.

In Figure 6, the per-unit values of three phase back-EMF are calculated by the rotor position. i_a^* and i_b^* are the per-unit values of given phase A and phase B currents, and they are calculated according to the back-EMF. Multiplying the given torque T_{set} by i_a^* and i_b^*, the actual given current i_{aset} and i_{bset} can be calculated. T_{set} is the output of velocity loop. Based on the PI regulator composed of the actual given and feedback currents, u_a and u_b is produced. u_c can be derived from u_a, u_b and bus voltage. Six drive signals with dead band are produced by the PWM modular, and the signals drive the BLDCM through power current.

In Figure 7, the given current i_{set} is the output of velocity loop, and i_f is the feedback current calculated by the rotor position and two phase current. Based on the PI regulator composed of i_{set} and i_f, the given signal of PWM modular is produced. Six drive signals is produced by logic modular according to the PWM and rotor position. Power current is driven by the six drive signals.

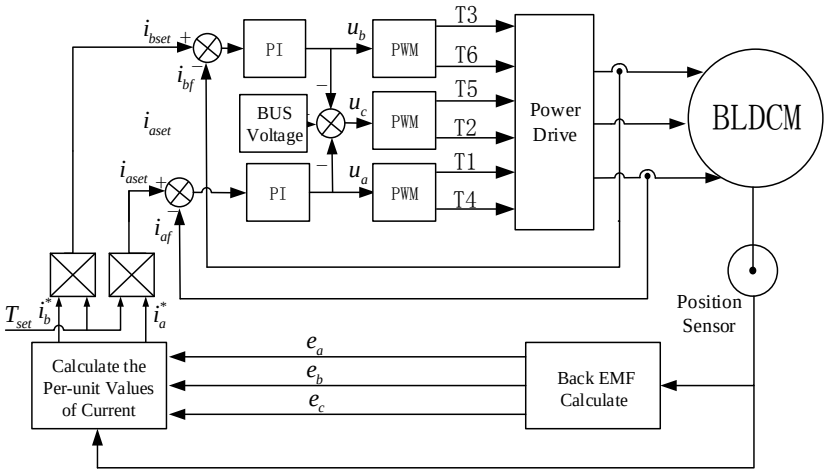

Figure 6. Control diagram of COC.

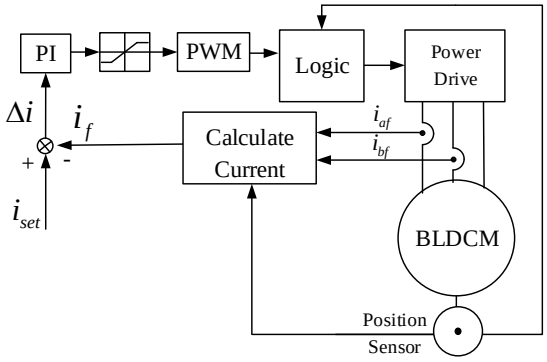

Figure 7. Control diagram of square-wave current control (SWC).

5.2. Experiment Result

In the experiment, load torque and bus voltage are set to the rated values. Switching frequency is 20 kHz. The reference velocities are set to 1500 r/min and 3000 r/min respectively.

When the reference velocity is 1500 r/min, the test waveforms are shown in Figure 8 with SWC and Figure 9 with COC respectively.

In Figure 8, the phase currents are similar to square waves, and have two ripples during conduction region for the non-ideal trapezoidal back-EMF. However, the non-commutation current curves in during the commutation region. Commutation torque ripples 6 times every 20 ms.

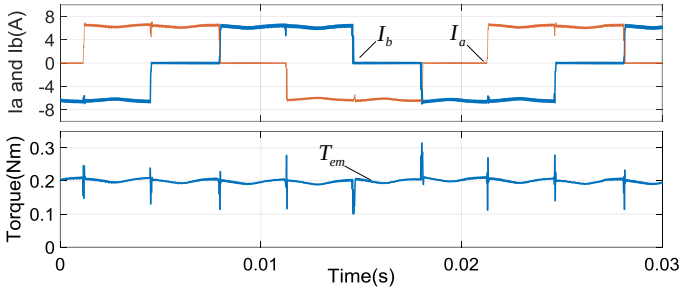

Figure 8. Test waveforms at the speed of 1500 r/min with SWC.

In Figure 9, the phase currents are continuous and similar to that of Figure 2. In the commutation region, the phase current are smooth and commutation torque ripple is reduced. The torque ripple also concludes elements affected by the sampling errors of phase current and non-ideal trapezoidal back-EMF.

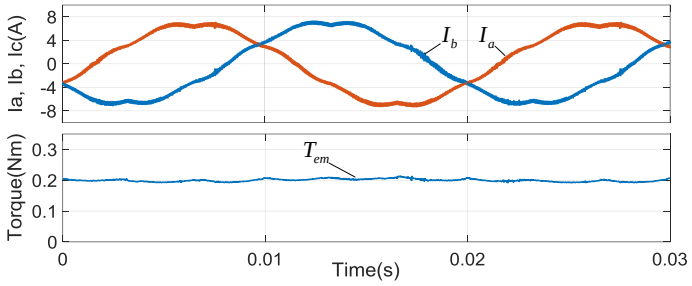

Figure 9. Test waveforms at the speed of 1500 r/min with COC.

When the reference velocity is 3000 r/min, the test waveforms are shown in Figure 10 with SWC and Figure 11 with COC. In Figure 10, commutation torque ripple increases with the increasing of velocity. While in Figure 11, commutation torque ripple is still reduced.

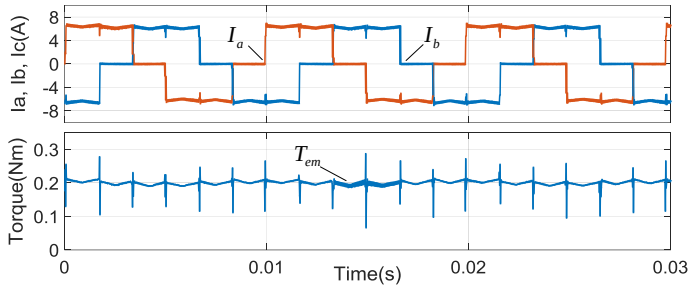

Figure 10. Test waveforms at the speed of 3000 r/min with SWC.

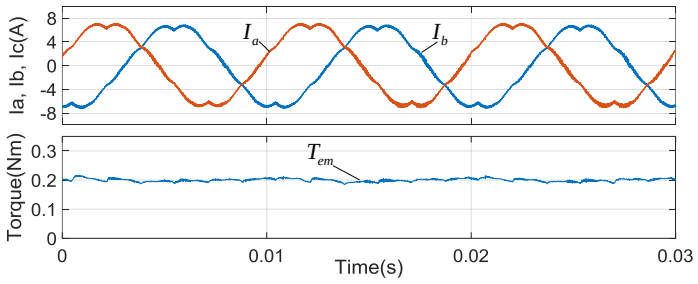

Figure 11. Test waveforms at the speed of 3000 r/min with COC.

The waveforms of torque are enlarged in Figure 12. In SWC, torque ripples are affected by commutation events, PWM, the sampling errors and non-ideal trapezoidal back-EMF. The commutation torque ripple increasing with the rising of velocity is the main element. Other torque ripples having little relation to velocity are the minor. In COC, the ranges of torque ripples are mainly the same in both 1500 r/min and 3000 r/min. Commutation torque ripple is reduced. The results are shown in Table 3.

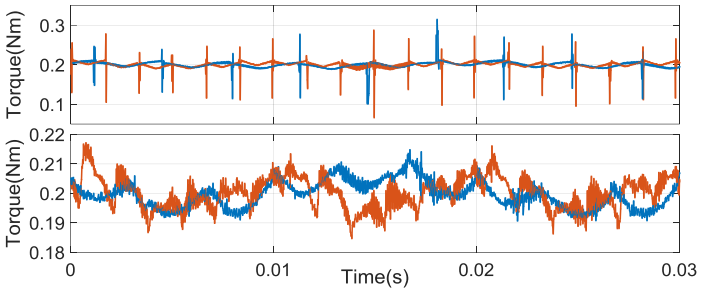

Figure 12. Test waveforms of torque: (**up**) with SWC (red line: 3000 r/min; blue line: 1500 r/min); (**down**) with COC (red line: 3000 r/min; blue line: 1500 r/min).

Table 3. Torque ripple comparison of SWC and COC.

Type	Velocity (r/min)	Commutation Ripple (Nm)	Other Ripple (Nm)
SWC	1500	0.115	0.008
COC	1500	0.014	0.008
SWC	3000	0.135	0.008
COC	3000	0.016	0.009

6. Conclusions

BLDCM has the disadvantage of the high commutation torque ripple, which limits its application in electric vehicles and servo systems. Analysis shows that the torque ripple is induced by the asynchrony of the current vector and the back-EMF vector in SWC. This is because the infinite velocity and constant modulus of the current vector is demanded in the commutation region by the asynchrony. However, the velocity is limited and the modulus is non-constant for the limited current change rates. A COC method in the natural a–b–c reference frame is proposed in the paper, which can keep the current vector and the back-EMF vector rotating synchronously. In COC, the modulus and velocity of the current vector demanded are minimum in the commutation region. The current change rates are reduced for the lowest modulus and the velocity of the current vector in the commutation region. The commutation torque ripple is minimum. Finally, the experimental results show that the COC method can reduce the commutation torque ripple in a wide speed range.

Acknowledgments: This work was supported in part by Shaanxi Key Research Project (2017GY-048).

Author Contributions: Bo Tan propose the COC method and designed the experiments; Lu Zhang and Bo Tan performed the experiments; Zhiguang Hua and Chun Fang analyzed the data and wrote the paper.

Conflicts of Interest: The authors declare no conflict of interest.

References

1. Pillay, P.; Krishnan, R. Application characteristics of permanent magnet synchronous and brushless DC motors for servo drives. *IEEE Trans. Ind. Appl.* **1991**, *27*, 986–996. [CrossRef]
2. Fang, J.C.; Zhou, X.X.; Liu, G. Precise Accelerated Torque Control for Small Inductance Brushless DC Motor. *IEEE Trans. Power Electron.* **2013**, *28*, 1400–1412. [CrossRef]
3. Shi, J.; Li, T.C. New Method to Eliminate Commutation Torque Ripple of Brushless DC Motor With Minimum Commutation Time. *IEEE Trans. Ind. Electron.* **2013**, *60*, 2139–2146. [CrossRef]
4. Xia, C.L.; Xiao, Y.W.; Chen, W.; Shi, T.N. Torque Ripple Reduction in Brushless DC Drives Based on Reference Current Optimization Using Integral Variable Structure Control. *IEEE Trans. Ind. Electron.* **2014**, *61*, 738–752. [CrossRef]
5. Xia, C.L.; Wang, Y.F.; Shi, T.N. Implementation of Finite-State Model Predictive Control for Commutation Torque Ripple Minimization of Permanent-Magnet Brushless DC Motor. *IEEE Trans. Ind. Electron.* **2013**, *60*, 896–905. [CrossRef]

6. Li, X.M.; Xia, C.L.; Cao, Y.F.; Chen, W.; Shi, T.N. Commutation Torque Ripple Reduction Strategy of Z-Source Inverter Fed Brushless DC Motor. *IEEE Trans. Power Electron.* **2016**, *31*, 7677–7690. [CrossRef]
7. Xu, Y.X.; Wei, Y.Y.; Wang, B.C.; Zou, J.B. A Novel Inverter Topology for Brushless DC Motor Drive to Shorten Commutation Time. *IEEE Trans. Ind. Electron.* **2016**, *63*, 796–807. [CrossRef]
8. Viswanathan, V.; Jeevananthan, S. Approach for torque ripple reduction for brushless DC motor based on three-level neutral-point-clamped inverter with DC-DC converter. *IET Power Electron.* **2015**, *8*, 47–55. [CrossRef]
9. Li, Z.G.; Gao, X.F.; Wang, J.H.; Zhang, C.J. Phase back EMF space vector oriented control of brushless DC motor for torque ripple minimization. In Proceedings of the 2016 IEEE 8th International Power Electronics and Motion Control Conference, Hefei, China, 22–25 May 2016; pp. 2564–2570.
10. Le-Huy, H.; Perret, R.; Feuillet, R. Minimization of Torque Ripple in Brushless DC Motor Drives. *IEEE Trans. Ind. Appl.* **1986**, 748–755. [CrossRef]
11. Bertoluzzo, M.; Buja, G.; Keshri, R.K.; Menis, R. Sinusoidal Versus Square-Wave Current Supply of PM Brushless DC Drives: A Convenience Analysis. *IEEE Trans. Ind. Electron.* **2015**, *62*, 7339–7349. [CrossRef]
12. Park, S.J.; Park, H.W.; Lee, M.H.; Harashima, F. A new approach for minimum-torque-ripple maximum-efficiency control of BLDC motor. *IEEE Trans. Ind. Electron.* **2000**, *47*, 109–114. [CrossRef]
13. Buja, G.; Bertoluzzo, M.; Keshri, R.K. Torque Ripple-Free Operation of PM BLDC Drives With Petal-Wave Current Supply. *IEEE Trans. Ind. Electron.* **2015**, *62*, 4034–4043. [CrossRef]
14. Gatto, G.; Marongiu, I.; Perfetto, A.; Serpi, A. Brushless DC generator controlled by constrained predictive algorithm. In Proceedings of the 2010 IEEE International Symposium on Industrial Electronics, Bari, Italy, 4–7 July 2010; pp. 1224–1229.
15. Damiano, A.; Deiana, F.; Fois, G.; Gatto, G.; Marongiu, I.; Serpi, A.; Perfetto, A. Performance comparison between two-phase-on and three-phase-on operation of Brushless DC drives. In Proceedings of the 2014 International Symposium on Power Electronics, Electrical Drives, Automation and Motion, Ischia, Italy, 18–20 June 2014; pp. 489–494.
16. Serpi, A.; Fois, G.; Porru, M.; Damiano, A.; Marongiu, I. Space vector control of permanent Magnet Brushless DC Machines. In Proceedings of the 2016 XXII International Conference on Electrical Machines, Lausanne, Switzerland, 4–7 September 2016; pp. 1194–1200.